1999-05

Uncertainty of the South China Sea prediction using NSCAT and NCEP winds during tropical storm Ernie 1996

Liu, W. Timothy

Uncertainty of South China Sea prediction using NSCAT and National Centers for Environmental Prediction winds during tropical storm Ernie, 1996

Peter C. Chu

Department of Oceanography, Naval Postgraduate School, Monterey, California

Shihua Lu

Institute of Plateau Atmospheric Physics, Academia Sinica, Lanzhou, China

W. Timothy Liu

Jet Propulsion Laboratory, Pasadena, California

Abstract. Error propagation from winds to ocean models was numerically investigated using the Princeton Ocean Model (POM) for the South China Sea with 20-km horizontal resolution and 23 σ levels conforming to a realistic bottom topography during the lifetime of tropical cyclone Ernie (November 4-18, 1996). Numerical integration was divided into preexperimental and experimental stages. The preexperiment phase generates the initial conditions on November 1 for the sensitivity experiment. During the experimental stage the POM was integrated from November 1 to 30, 1996 under National Centers for Environmental Prediction (NCEP) reanalyzed surface fluxes along with two surface wind data sets, namely, the daily averaged interpolated NASA scatterometer winds and the NCEP winds. The relative root-mean-square differences fluctuate from 0.5 to 1.0 for winds, 0.25 to 0.7 for surface elevations, 0.47 to 1.02 for surface currents, and 0 to 0.23 for surface temperatures. This indicates that the model has less uncertainty overall than the wind fields used to drive it, which in turn suggests that the ocean modeling community may progress without waiting for the atmospheric modelers to build the perfect forecast model.

1. Introduction

Several important questions in ocean modeling need to be answered: How does error propagate from winds to ocean? Will the wind error be amplified or damped after it enters the ocean models? A possible way to deal with these problems is to run an ocean model with two different wind data sets, then to analyze the variability of the two ocean model fields versus the variability of the two wind fields. Here we chose the Princeton Ocean Model (POM) for the South China Sea (SCS) for such a study.

The SCS is a semienclosed, tropical sea located between the Asian land mass to the north and west, the Philippine Islands to the east, Borneo to the southeast, and Indonesia to the south (Figure 1), a total area of 3.5×10^6 km². It includes the shallow Gulf of Thailand and connections to the East China Sea (through the Taiwan Strait), to the Pacific Ocean (through the Luzon Strait), to the Sulu Sea (through the Mindoro Strait), to the Java Sea (through the Gasper and Karimata Straits), and to the Indian Ocean (through the Strait of Malacca). All of these straits are shallow, except the Luzon Strait, whose maximum depth is 1800 m. The complex topography includes the broad shallows of the Sunda Shelf in the south/southwest; the continental shelf of the Asian landmass in the north, extending from the Gulf of Tonkin to the Taiwan Strait; a deep, elliptical shaped basin in the center, and numerous reef islands and underwater plateaus scattered throughout. The shelf that extends from the Gulf of Tonkin to the Taiwan Strait is consistently near 70 m deep and averages 150 km in width; the central deep basin is 1900 km along its major axis (northeast-southwest) and approximately 1100 km along its minor axis and extends to over 4000 m deep. The Sunda Shelf is the submerged connection between southeast Asia, Malaysia, Sumatra, Java, and Borneo and is 100 m deep in the middle; the center of the Gulf of Thailand is about 70 m deep.

The SCS is subjected to a seasonal monsoon system [*Wyrtki*, 1961; *Chu et al.*, 1997a, 1998a; *Metzger*
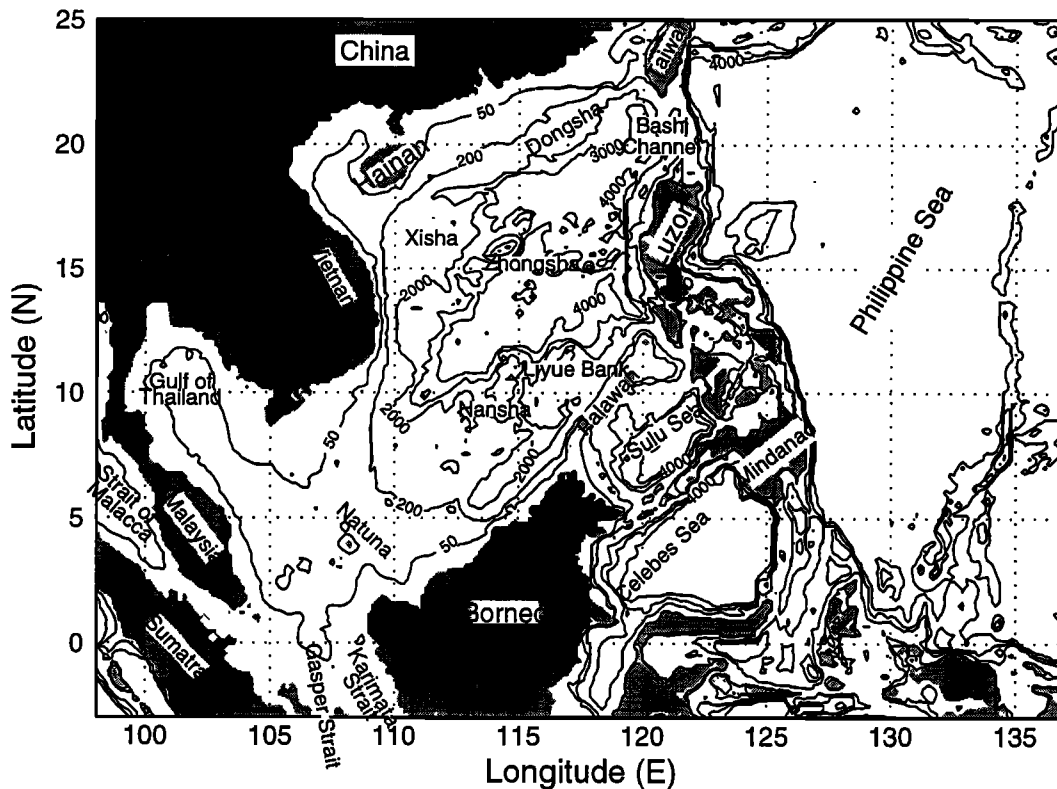
Figure 1. Bathymetry (meter) and coastline of the South China Sea (SCS).

and Hurlburt, 1996]. From April to August the weaker southwesterly summer monsoon winds result in a wind stress of more than 0.1 N m^{-2} (Figure 2a), which drives a northward coastal jet off Vietnam and anticyclonic circulation in the SCS (Figure 3, top). From November to March the stronger northeasterly winter monsoon winds correspond to a maximum wind stress of nearly 0.28 N m^{-2} (Figure 2b), causing a southward coastal jet and cyclonic circulation in the SCS (Figure 3, bottom). The transitional periods are marked by highly variable winds and surface currents.

More tropical cyclones form over the western North Pacific and SCS regions than in any other ocean basin, with an average of about 26 per year [*McBride,* 1995]. Although highly seasonal, this is the only region in which tropical cyclones have been observed in all months of the year. The primary reason for this high incidence of occurrence is the persistently warm sea surface temperatures (SST) and the location of the intertropical convergence zone (ITCZ). The ITCZ occurs as a convergence zone in the westerly monsoon flow, known as the monsoon trough [*Gray,* 1968]. The trough is the shear line separating the monsoonal westerlies from the trade easterlies and is a preferred region for tropical cyclone development. The tropical cyclone Ernie in 1996 was selected since it traveled through the whole SCS during November 1996. More importantly, we have both satellite and reanalyzed wind data for the duration of tropical cyclone Ernie.

The National Aeronautics and Space Administration (NASA) scatterometer (NSCAT) was successfully launched into a near-polar and Sun-synchronous orbit on the Japanese Advanced Earth Observing Satellite (ADEOS 1) in August 1996. About 9 months of data were collected before the failure of ADEOS. From NSCAT observations, surface wind vectors (speed and direction) at 10-m height were derived at 25-km spatial resolution, covering approximately 77% of the Earth's oceans in 1 day and 87% in 2 days, under both clear and cloudy conditions. The NSCAT observations were interpolated objectively by the method of successive corrections to form a uniformly gridded wind field, with 0.5° latitude by 0.5° longitude and 12-hour resolution [*Tang and Liu,* 1996; *Liu et al.,* 1998].

Two surface wind data sets were chosen for the study, namely, the NSCAT winds and the National Centers for Environmental Prediction (NCEP) T63 (equivalent to 1.875° × 1.875° resolution) reanalyzed winds. The daily mean data were used for simplicity since we are only interested in the error propagation.

The outline of this paper is as follows. A description of tropical cyclone Ernie 1996 is given in section 2. A depiction of numerical experiments is given in section 3. Statistical analyses are presented in section 4. Discrepancy between NSCAT and NCEP surface winds is described in section 5. SCS model response is given in section 6. In section 7 we present our conclusions.
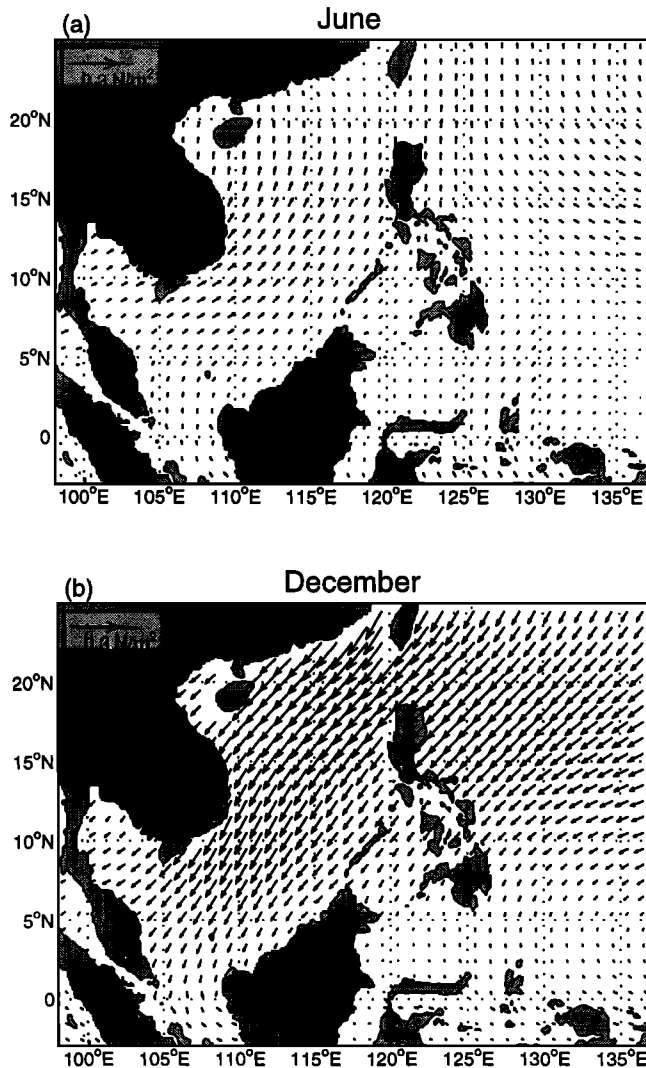
Figure 2. Climatological wind stress (N m^{-2}) for (a) June and (b) December.

2. Tropical Cyclone Ernie, 1996

Tropical cyclone Ernie formed initially about 1300 km to the east of the Philippine island of Mindanao on November 4, 1996. After formation, Ernie slowly intensified as it tracked westward through the Philippine Sea toward the central Philippine islands. Figure 4 shows the track of Ernie, which was obtained from the Joint Typhoon Warning Center (JTWC) on Guam. On November 6, Ernie made landfall over Mindanao and intensified to 18 m s^{-1}, tropical storm strength. Ernie continued moving westerly through the Philippine Islands, intensifying at a slow rate owing to interaction with the land. The storm entered the SCS on November 7 and reached an intensity of 25 m s^{-1}. On November 8, Ernie became quasi-stationary over the eastern SCS and began losing intensity when midlevel steering flow diminished and a strong, low-level monsoonal flow developed. Tropical depression (TD) 39W, which had formed over Luzon to the northeast of Ernie during the previ-

ous day, began interacting with Ernie at this time, and late on November 8, Ernie began moving northerly toward this circulation. Ernie merged with TD 39W and continued moving northerly, slowly intensifying from its low wind speed of 15 m s^{-1} after merger to 23 m s^{-1}. On November 11, midlevel steering flow again diminished and Ernie commenced slowly drifting southerly toward Luzon, approximately 270 km to the southeast. On November 12, Ernie was over Luzon and midlevel steering flow reintensified, causing the system to begin moving to the west-southwest, back into the SCS. Ernie continued moving to the west-southwest over the next 4 days, passing over the southern tip of Vietnam and slowly weakening to 15 m s^{-1}. Ernie tracked into the Gulf of Thailand and then finally into the eastern Bay of Bengal, where it dissipated over water on November 18.

3. Numerical Experiments

3.1. Model Description

POM is the three-dimensional primitive equation model developed by *Blumberg and Mellor* [1987] with hydrostatic and Boussinesq approximations and has the following features: (1) a staggered C grid, (2) σ coordinates in the vertical, (3) a free surface, (4) a second-order turbulence closure model for vertical viscosity [*Mellor and Yamada*, 1982], (5) horizontal diffusivity coefficients calculated by the *Smagorinsky* [1963] parameterization, and (6) split time steps for barotropic (25 s) and baroclinic modes (900 s).

The model was specifically designed to accommodate mesoscale phenomena commonly found in estuarine and coastal oceanography. Tidal forcing and river outflow were not included in this application of the model. However, the seasonal variation in sea surface height, temperature, salinity, circulation, and transport are well represented by the model data. From a series of numerical experiments [*Chu et al.*, 1998b], the effects of wind forcing and lateral boundary transport on the SCS warm-core and cool-core eddies are analyzed, yielding considerable insight into the external factors affecting the region oceanography.

In this study we use a rectilinear grid with horizontal spacing of 20 km by 20 km resolution and 23 nonuniform vertical σ coordinate levels (Table 1). The model domain is from 3.06°S to 25.07°N and 98.84°E to 121.16°E, which encompasses the SCS and the Gulf of Thailand, and uses realistic bathymetry data from the Naval Oceanographic Office Digital Bathymetry Data Base with 5 min by 5 min resolution (DBDB5). Consequently, the model contains 125 × 162 × 23 horizontally fixed grid points (Figure 5). The horizontal diffusivities are modeled using the *Smagorinsky* [1963] form, with the coefficient chosen to be 0.2 for this application. The bottom stress is assumed to follow a quadratic law, and the drag coefficient is specified as 0.0025 [*Blumberg and Mellor*, 1987].
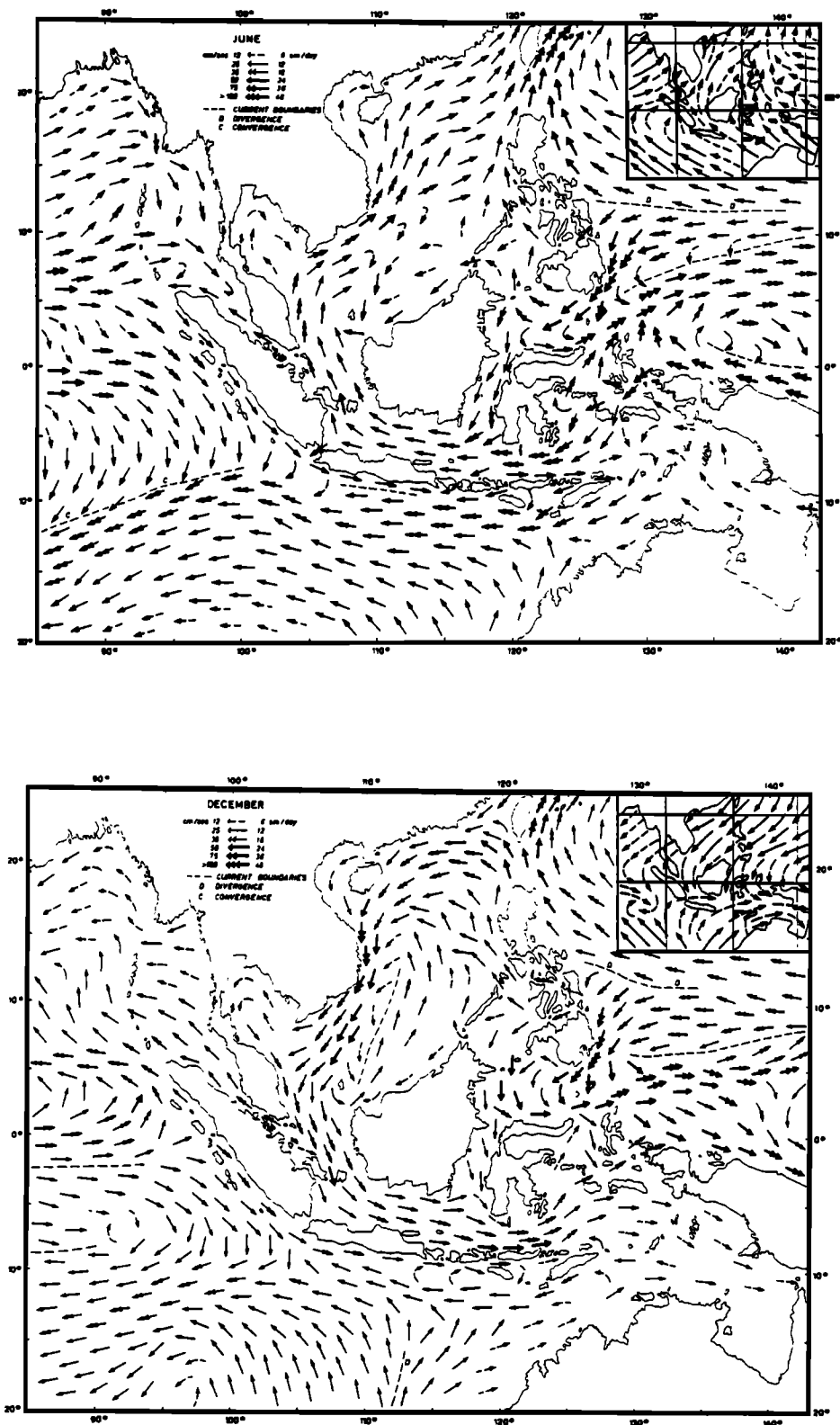
Figure 3. Surface circulation pattern of the South China Sea for (top) June and (bottom) December [from *Wyrtki*, 1961].
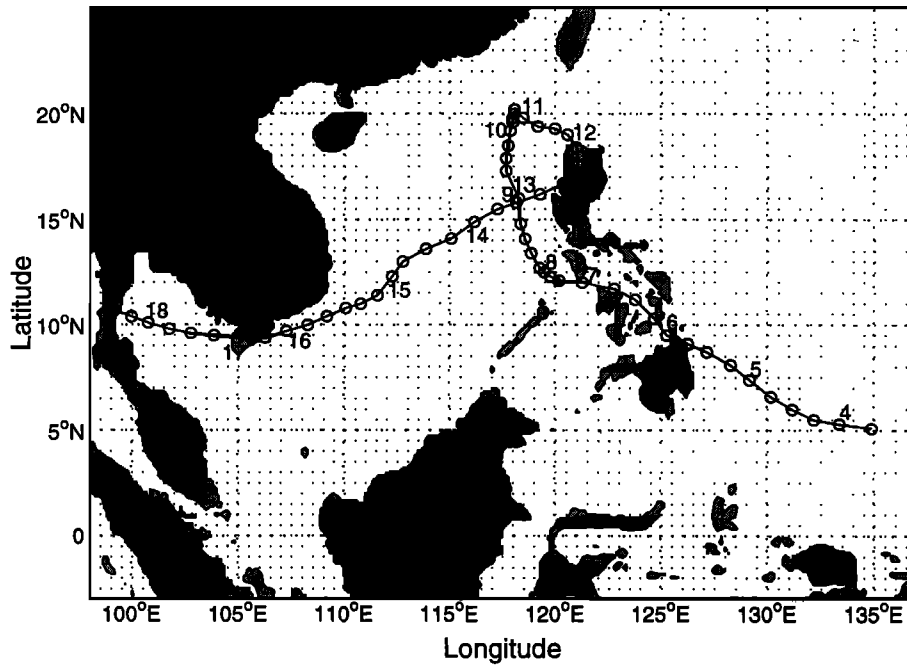
Tropical Storm Ernie (Nov 1996) Best Track

Figure 4. Track of tropical cyclone Ernie, November 1996.

3.2. Experiment Design

Numerical integration was divided into preexperimental and experimental stages. During the preexperimental stage we integrated the POM for 43 months using temperature and salinity climatological fields [*Lev-*

Table 1. Twenty-three σ Levels

σ Level	σ Value
1	0
2	-0.0125
3	-0.025
4	-0.05
5	-0.1
6	-0.15
7	-0.2
8	-0.25
9	-0.3
10	-0.35
11	-0.4
12	-0.45
13	-0.5
14	-0.55
15	-0.6
16	-0.65
17	-0.7
18	-0.75
19	-0.8
20	-0.85
21	-0.9
22	-0.95
23	-1

itus and Boyer, 1994; *Levitus et al.*, 1994], climatological monthly mean wind stresses [*Hellerman and Rosenstein*, 1983], restoring-type surface salt and heat fluxes, and observational oceanic inflow/outflow at the open boundaries, and we started from zero velocity and April temperature and salinity fields. The fields at the end of the integration period were taken as the initial fields (November 1) for the sensitivity study. During the experimental stage, POM was integrated for another month under NCEP T63 (equivalent to 1.875° × 1.875° resolution) reanalyzed surface fluxes along with two surface wind data sets, namely, the daily averaged interpolated NSCAT winds and the NCEP T63 winds. All the surface forcing data used were from November 1 to 30, 1996.
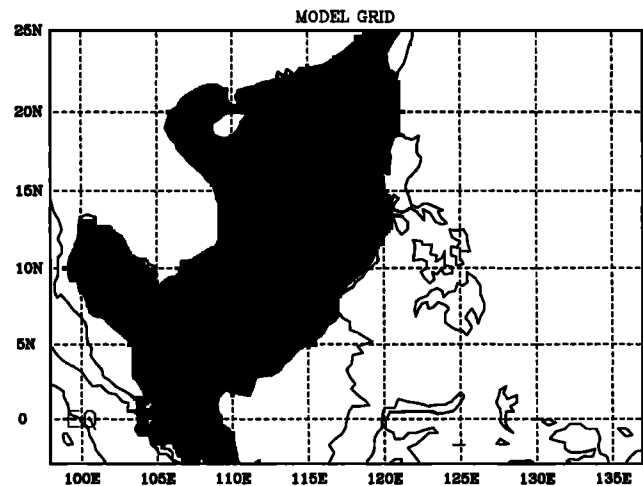

Figure 5. Horizontal model grids.

Table 2. Bimonthly Variation of Volume Transport at Lateral Open Boundaries [a]

	Feb.	April	June	Aug.	Oct.	Dec.
Gaspar- Karimata Straits	4.4	0.0	-4.0	-3.0	1.0	4.3
Luzon Strait	-3.5	0.0	3.0	2.5	-0.6	-3.4
Taiwan Strait	-0.9	0.0	1.0	0.5	-0.4	-0.9

[a] Values are in Sverdrups. Positive/negative values mean outflow/inflow and were taken from *Wyrtki* [1961].

3.3. Atmospheric Forcing

3.3.1. Wind forcing. The atmospheric forcing for the SCS application of the POM includes mechanical and thermodynamic forcing. The wind forcing is depicted by

$$\rho_0 K_M (\partial u/\partial z, \partial v/\partial z)_{z=0} = (\tau_{0x}, \tau_{0y}) \qquad (1)$$

where (u, v) and (τ_{0x}, τ_{0y}) are the two components of the water velocity and wind stress vectors, respectively; ρ_0 is the reference density; and K_M is the vertical mixing coefficient for momentum.

From a climatological point of view the SCS experiences two monsoons, winter and summer, every year. During the winter monsoon season a cold northeast wind blows over the SCS (Figure 2a) as a result of the Siberian high-pressure system located over the east Asian continent. Radiative cooling and persistent cold air advection maintain cold air over the SCS. The northeast-southwest oriented jet stream is positioned at the central SCS. Such a typical winter monsoon pattern lasts nearly 6 months (November to April). During the summer monsoon season a warm and weaker southwest wind blows over SCS (Figure 2b). Such a typical sum-

mer monsoon pattern lasts nearly 4 months (mid-May to mid-September).

During the preexperiment stage the wind stress at each time step is interpolated from monthly mean climate wind stress [*Hellerman and Rosenstein*, 1983], which was taken as the value at the middle of the month. During the experiment stage we used the two daily surface wind data sets (NSCAT and NCEP) to force the SCS POM model.

3.3.2. Thermohaline forcing. Surface thermal forcing is depicted by

$$K_H \frac{\partial \theta}{\partial z} = \alpha_1 (\frac{Q_H}{\rho c_p}) + \alpha_2 C (\theta_{OBS} - \theta) \qquad (2)$$

$$K_S \frac{\partial S}{\partial z} = \alpha_1 Q_S + \alpha_2 C (S_{OBS} - S) \qquad (3)$$

where K_H and K_S are the vertical mixing coefficients for temperature and salinity, respectively; θ_{OBS} and S_{OBS} are the observed potential temperature and salinity, respectively; c_p is the specific heat; and Q_H and Q_S are surface net heat and salinity fluxes, respectively. The relaxation coefficient C is the reciprocal of the restoring time period for a unit volume of water. The parame-
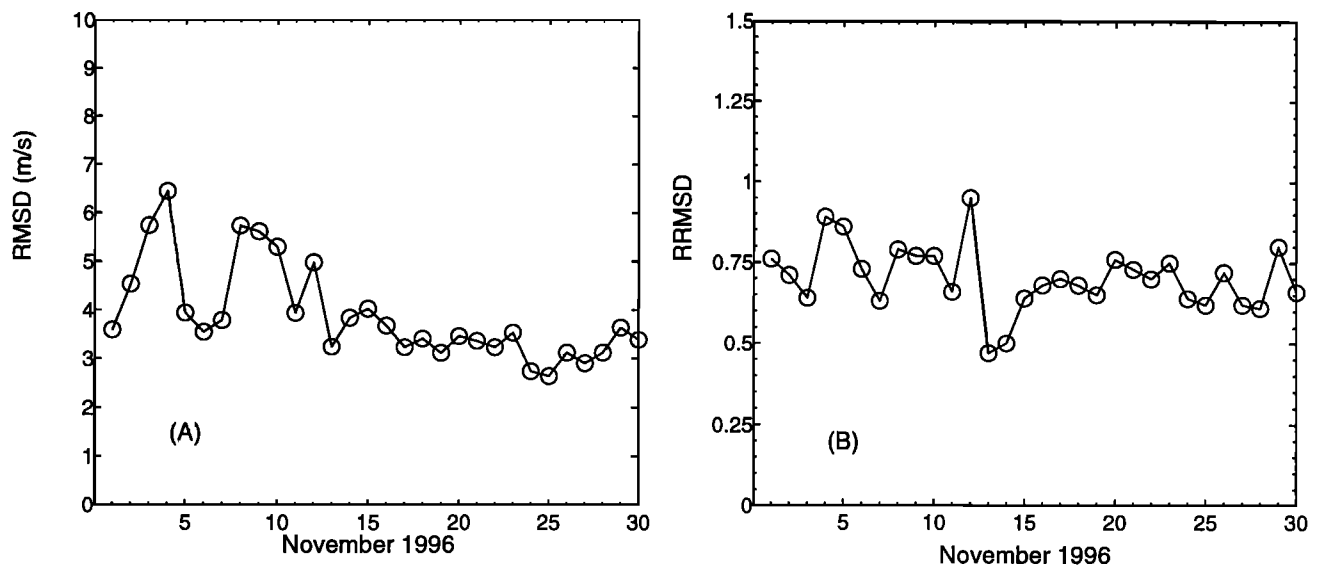

Figure 6. Temporally varying (a) root-mean-square difference (rmsd) and (b) relative root-mean-square difference (rrmsd) between daily mean NASA scatterometer (NSCAT) and National Centers fot Environmental Prediction (NCEP) winds over SCS.

ters (α_1, α_2) are (0,1)-type switches: $\alpha_1 = 1$, $\alpha_2 = 0$, would specify only if flux forcing is applied; $\alpha_1 = 0$, $\alpha_2 = 1$, would specify that only restoring-type forcing is applied. The relaxation coefficient C is taken to be 0.7 m day^{-1}, which is equivalent to a relaxation time of 43 days for an upper layer 30 m thick [*Chu et al.*, 1996]. Here we used restoring-type forcing for the pre-experiment $(\alpha_1 = 0, \alpha_2 = 1)$ and flux forcing for the experiment $(\alpha_1 = 1, \alpha_2 = 0.)$

3.4. Lateral Boundary Conditions

Solid lateral boundaries, i.e., the modeled ocean bordered by land, were defined using a free slip condition for velocity and a zero gradient condition for temperature and salinity. No advective or diffusive heat, salt, or velocity fluxes occur through these boundaries.

Open boundaries, where the numerical grid ends but the fluid motion is unrestricted, were treated as radiative boundaries. Volume transport through the Luzon Strait, Taiwan Strait, and Gasper/Karimata Strait was defined according to observations (Table 2). However, the Balabac Channel, Mindoro Strait, and Strait of Malacca are assumed to have zero transport. When the water flows into the model domain, temperature and salinity at the open boundary are likewise prescribed from the climatological data [*Levitus and Boyer*, 1994]. When water flows out of the domain, the radiation condition was applied,

$$\frac{\partial}{\partial t}(\theta, S) + U_n \frac{\partial}{\partial n}(\theta, S) = 0 \qquad (4)$$

where U_n is the normal velocity at the boundary; and the subscript n is the direction normal to the boundary.

4. Statistical Analyses

The uncertainty of SCS in the two wind data sets was analyzed using correlation analysis and root-mean-square difference (rmsd). Let (x_i, y_j) and σ be the horizontal and vertical coordinates, respectively, of a model grid. For a given time t, let $\psi_{\rm NSCAT}(x_i, y_j, \sigma, t)$ and $\psi_{\rm NCEP}(x_i, y_j, \sigma, t)$ represent two sets of wind and model output. For surface wind data and two-diemnsional output such as surface elevation, we set $\sigma = 0$. Three parameters used to identify difference are root-mean-square (rms) difference, relative rms difference, and cor-

relation coefficient (CC). The rms difference represents the overall difference, the relative rms difference denotes the overall difference relative to the internal variability, and CC indicates the correlation between the two model data sets. Discrepancy between the two data sets is characterized by large values of rms difference and low values of CC.

4.1. The rms Difference

The rms difference between $\psi_{\rm NSCAT}(x_i, y_j, \sigma, t)$ and $\psi_{\rm NCEP}(x_i, y_j, \sigma, t)$ is defined by

$$\mathrm{rmsd}_\psi(\sigma, t) = \sqrt{\frac{1}{M} \sum_i \sum_j |\Delta\psi(x_i, y_j, \sigma, t)|^2} \qquad (5)$$

where

$$\Delta\psi(x_i, y_j, \sigma, t) = \psi_{\rm NSCAT}(x_i, y_j, \sigma, t) - \psi_{\rm NCEP}(x_i, y_j, \sigma, t) \qquad (6)$$

and M is the total number of horizontal grid points. The variable ψ can be either scalar or vector (wind and current). If ψ is a vector, $|(\Delta\psi)|$ in (5) means the modulus of the vector $\Delta\psi$.

4.2. Relative rms Difference

The relative rms difference (rrmsd) is the ratio between rmsd and standard deviation of the fields,

$$\mathrm{rrmsd}_\psi(\sigma, t) = \frac{\mathrm{rmsd}_\psi(\sigma, t)}{S_\psi(\sigma, t)} \qquad (7)$$

where the standard deviation $S_\psi(\sigma, t)$ is computed by

$$S_\psi(\sigma, t) = \sqrt{\frac{1}{M-1} \sum_i \sum_j \left|\psi_{\rm NCEP}(x_i, y_j, \sigma, t) - \overline{\psi_{\rm NCEP}(\sigma, t)}\right|^2} \qquad (8)$$

Here the overbar $\overline{()}$ indicates the horizontal mean, and the variable ψ can be either scalar or vector (wind and current).

4.3. Correlation Coefficient

The Pearson product-moment correlation coefficient between $\psi_{\rm NSCAT}(x_i, y_j, \sigma, t)$ and $\psi_{\rm NCEP}(x_i, y_j, \sigma, t)$ is computed through all the SCS horizontal model grids,

Table 3. Maximum Root-Mean-Square Differences of Various Parameters and Dates of Occurrence

	Maximum Value	Date in November
Surface winds, m s^{-1}	6.7	4
Surface elevation, cm	4.3	4, 30
Surface current, m s^{-1}	0.18	30
T $(\sigma = -0.025)$, ° C	0.52	30

$$CC(\sigma,t) = \frac{M \sum \psi_{\text{NSCAT}}\psi_{\text{NCEP}} - \left(\sum \psi_{\text{NSCAT}}\right)\left(\sum \psi_{\text{NCEP}}\right)}{\sqrt{\left[M \sum \psi_{\text{NSCAT}}^2 - \left(\sum \psi_{\text{NSCAT}}\right)^2\right]\left[M \sum \psi_{\text{NCEP}}^2 - \left(\sum \psi_{\text{NCEP}}\right)^2\right]}}$$

$$(9)$$

Since neither of the two model data sets is considered "true," the three parameters defined in this section, $\text{rmsd}_\psi(\sigma,t)$, $\text{rrmsd}_\psi(\sigma,t)$, and $CC(\sigma,t)$, cannot be considered as an error bias. They only show the difference between the two model results.

5. Discrepancy Between NSCAT and NCEP Surface Winds in November 1996

Before analyzing the data, both daily averaged NCEP and NSCAT wind data were interpolated into the ocean model grids. Quite surprisingly, the difference between the two wind fields is not negligible. The rmsd (Figure 6a) increases from 3.6 m s^{-1} on November 1 to a maximum value of 6.7 m s^{-1} on November 4, 1996 (Table 3), the day when the boundary current was strongest; and then fluctuates between 6.7 and 2.7 m s^{-1}. The rrmsd (Figure 6b) varies between 0.5 and 1, with a maximum value of 1.0 on November 12 (Table 4), indicating that the difference between the two wind data sets has the same order of magnitude as the internal variability. The value of 1 for rrmsd means that the difference between the two model results equals the model's internal variability.

Figure 7 shows the comparison between NSCAT and NCEP winds on November 4, 12, and 15 when rmsd exceeds 5 m s^{-1}. On November 4, both data sets show the establishment of the northeast monsoon in the northern SCS (110°-120°E, 16°-25°N) and the retreat of the southwest monsoon in the southern SCS. However, the NSCAT winds show a stronger retreat of the southwest monsoon than the NCEP winds. In the central SCS (5°-18°N) the southwest monsoon disappeared (appeared) in the NSCAT (NCEP) wind data. The difference between the two data sets has the same order of magnitude of the wind itself, i.e., 10-20 m s^{-1}. Moreover, the NCEP winds exhibit a strong convergence between the northeast and southwest monsoons near 14°N, but NSCAT winds do not. Such a large uncertainty on November 4 instead of when the cyclone was present may be associated with the monsoon reversal. During November 9-13, Ernie was in the quasi-

stationary stage, looping around west of Luzon Island (Figure 4). On November 12, Ernie was located at the north tip of Luzon. Both winds show the existence of a cyclone centered at the north tip of Luzon. Ernie was much stronger in the NSCAT winds than in the NCEP winds. After November 12, Ernie moved toward Vietnam. On November 15, Ernie was located at 12°N, 112°30'E (Figure 4). However, it was shifted toward south (8°N, 112°E) in both NSCAT and NCEP winds and was very weak in the NSCAT winds.

The correlation coefficient between daily NSCAT and NCEP wind components also fluctuates (Figure 8). During the lifetime of Ernie (November 4-18, 1996), CC fluctuated between 0.6 and 0.9 for the u component and between 0.42 and 0.92 for the v component. The minimum CC was determined to be 0.42 for the latitudinal component on November 4, 1996 (Table 5.)

6. SCS Model Response to the Uncertainty of Wind Forcing

Since the two surface wind data sets are quite different, we may ask how does the ocean respond to such a wind discrepancy? The emphasis here is to show the model uncertainty caused by the wind uncertainty. Thus we computed rmsd, rrmsd, and CC of model outputs (surface elevation, currents, and temperature) using NSCAT and NCEP winds to describe the uncertainty. We refer to the NSCAT run as the numerical simulation with the NSCAT winds and to the NCEP run as the numerical simulation with the NCEP winds.

6.1. Surface Elevation

Figure 9 shows the comparison between two surface elevation fields under NSCAT and NCEP wind forcing on November 4, 12, and 15. As Ernie was generated east of the South China Sea on November 4, 1996 (Figure 9a), both runs simulated surface depression in the deep SCS basin with a maximum value of 6 cm and produced sea surface setups along the southeast Chinese coast. The difference between the two runs on November 4 is

Table 4. Maximum Relative Root-Mean-Square Differences of Various Parameters and Dates of Occurrence

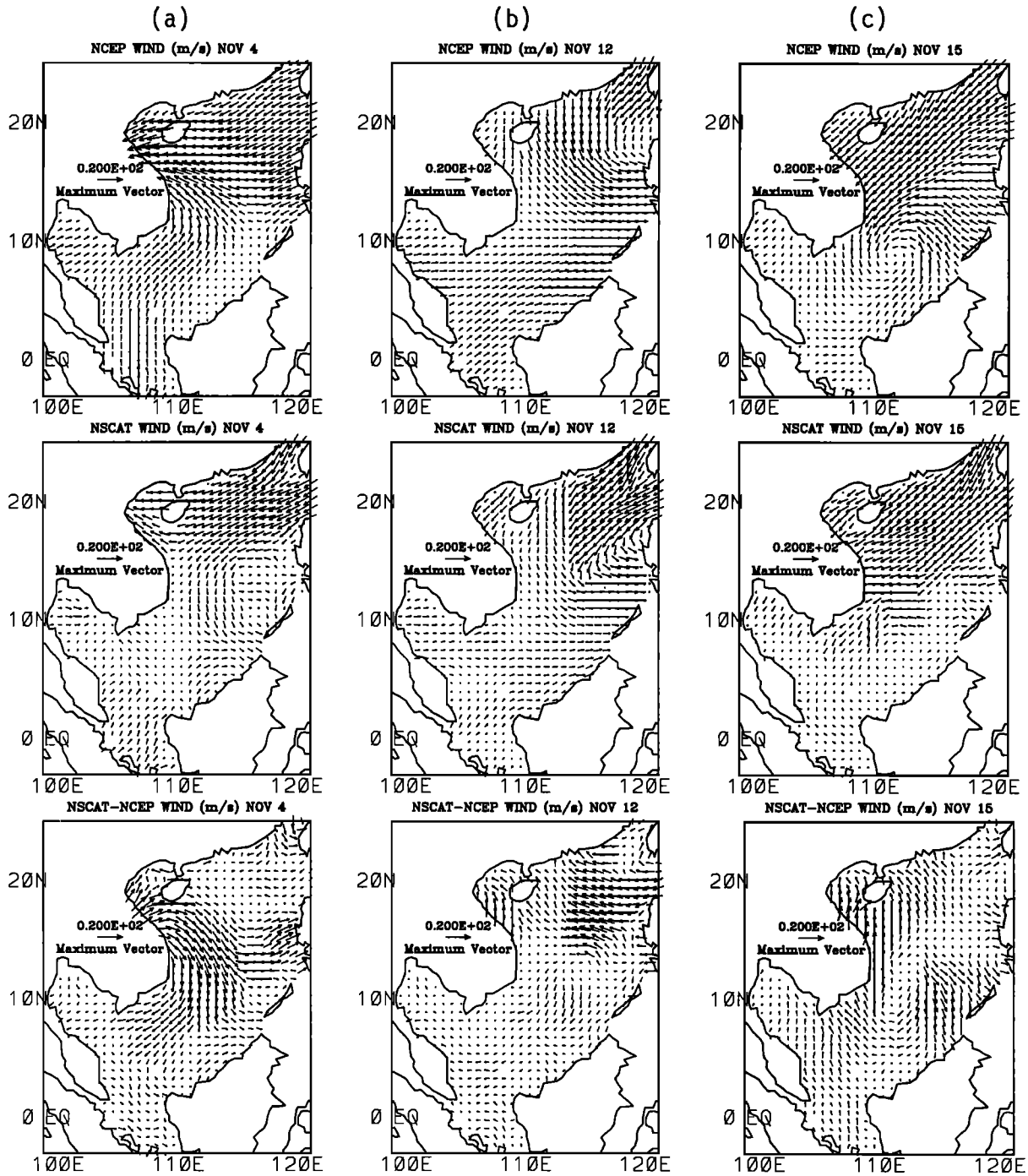|	Maximum Value	Date in November
Surface winds	1.0	12
Surface elevation	0.7	12
Surface current	1.02	4
Sea surface temperature	0.23	18

Figure 7. Comparison between interpolated NSCAT and NCEP wind vectors on November (a) 4, (b) 12, and (c) 15.
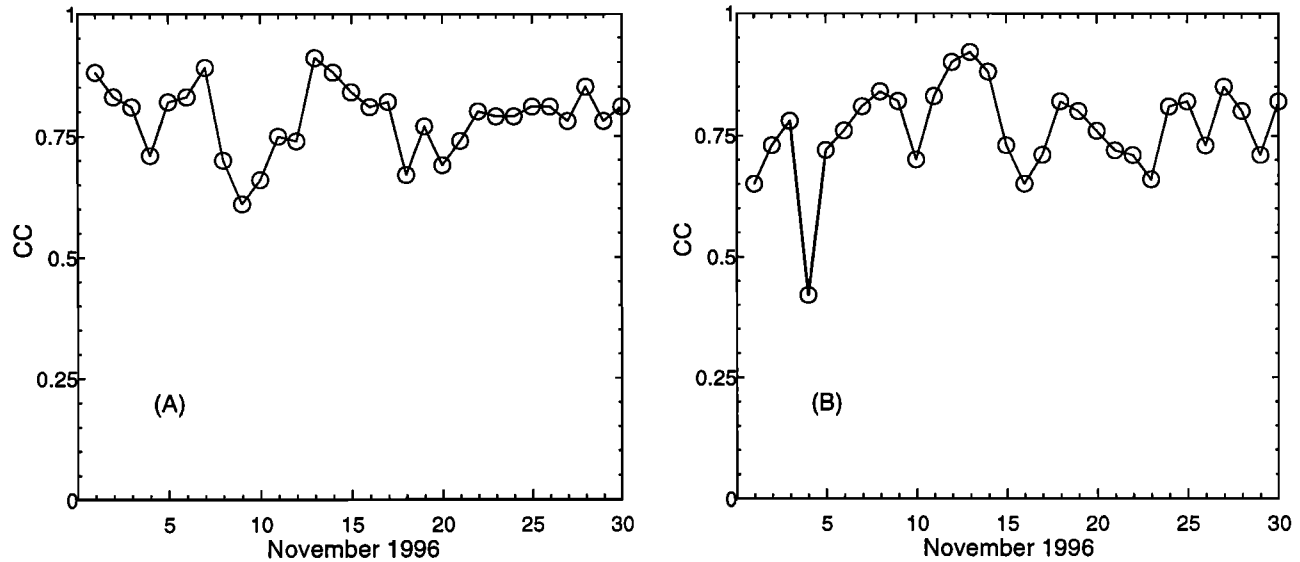
Figure 8. Correlation coefficient between daily mean interpolated NSCAT and NCEP winds for the (a) u and (b) v components.

small in the deep SCS basin (1 cm) and a little larger along the southeast Chinese coast (3 cm). During the period (November 10-13) when Ernie becomes quasi-stationary, the NSCAT run generated stronger depression in the SCS deep basin and stronger sea surface setups along the southeast Chinese coast than the NCEP run (Figure 9b). This is due to the stronger cyclone near Luzon presented by the NSCAT winds (Figure 7b). As Ernie approached the Vietnamese coast on November 15, the NSCAT run generated less depression (3 cm) south of 15°N than the NCEP run. This is caused by a weaker tropical cyclone presented in the NSCAT winds (Figure 7c).

The rmsd of surface elevation (Figure 10a) generally increases with time and has a maximum value of 4.3 cm on November 4 (the day when the western boundary current was strongest) and on November 30, 1996 (Table 3). The rrmsd of surface elevation (Figure 10b) fluctuates between 0.25 and 0.70 (Table 4) with several high values during the life span of Ernie: 0.66 on November 4, 0.7 on November 12, and 0.67 on November 13, and has relatively low values (0.3-0.41) after the disappearance of Ernie on November 19. The high value

of rrmsd (0.7 on November 12) indicates that the surface elevation difference between the two runs has almost the same order of magnitude as the internal variability (Table 4). The CC of surface elevation between the two runs fluctuates between 0.81 and 0.96 with a low correlation of 0.81 (Table 5) on November 12-13 (Figure 11), related to the high values of 3.5 cm for rmsd and 0.7 for rrmsd.

6.2. Currents

Figure 12 shows the comparison of the surface current vectors between NSCAT and NCEP runs. On November 4, the NSCAT run shows the establishment of the winter SCS circulation pattern (a southward coastal jet and cyclonic circulation) depicted in Figure 3, bottom; but the NCEP run does not show a typical winter SCS circulation pattern. There was no coastal jet along the southeast Chinese coast and no evident cyclone in the SCS basin. On November 12, Ernie was located near the north tip of Luzon (Figure 4). The NSCAT run shows a strong divergence in the northern SCS near the Luzon Strait (112°-120°E, 18°-22°N). The NCEP run does not show such a divergence. Difference between

Table 5. Minimum Correlation Coefficients of Various Parameters and Dates of Occurrence

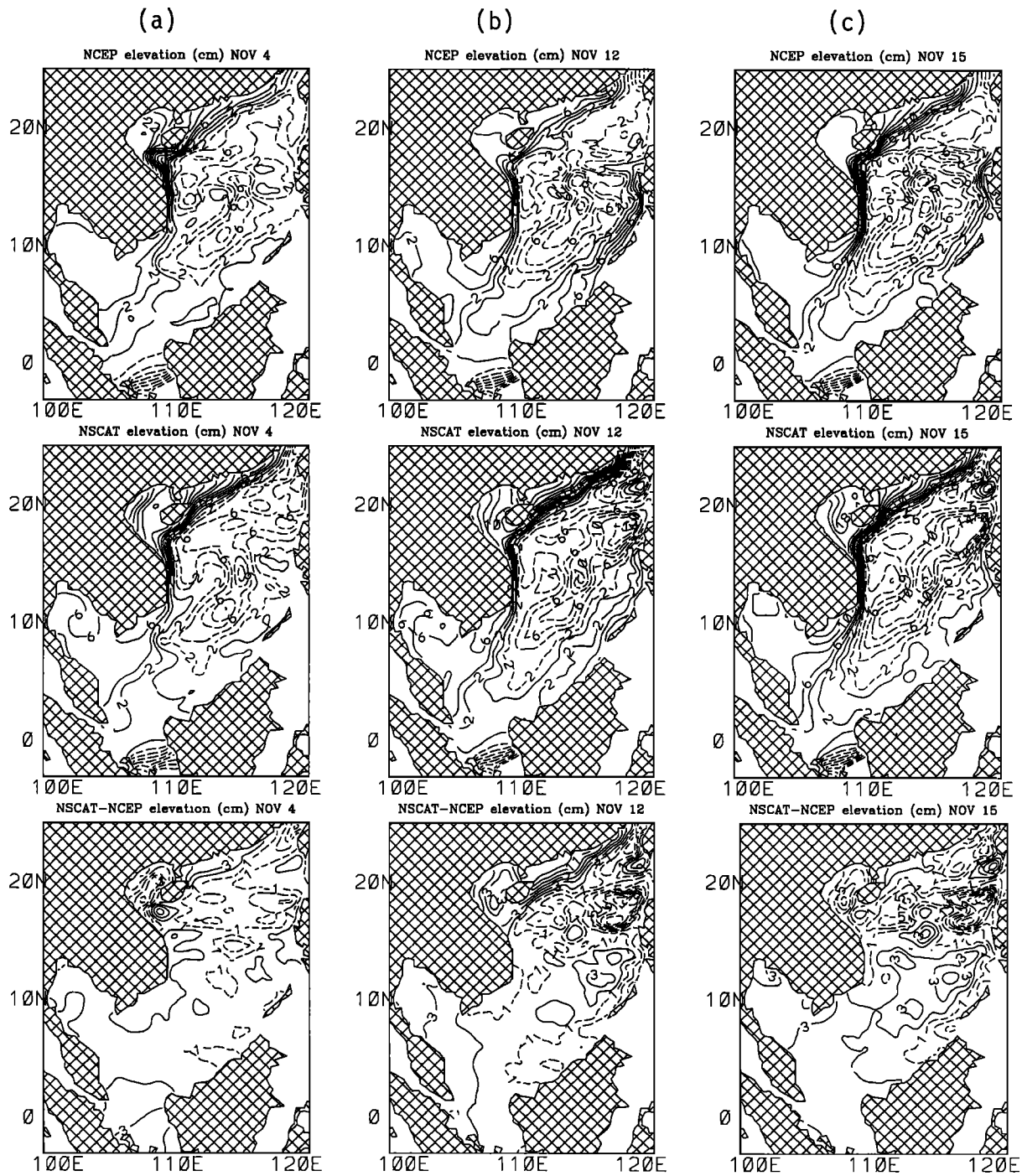|	Maximum Value	Date in November
Surface winds	0.42	4
Surface elevation	0.81	12-13
Surface current	0.59	4
Sea surface temperature	0.97	17, 23, 26-30

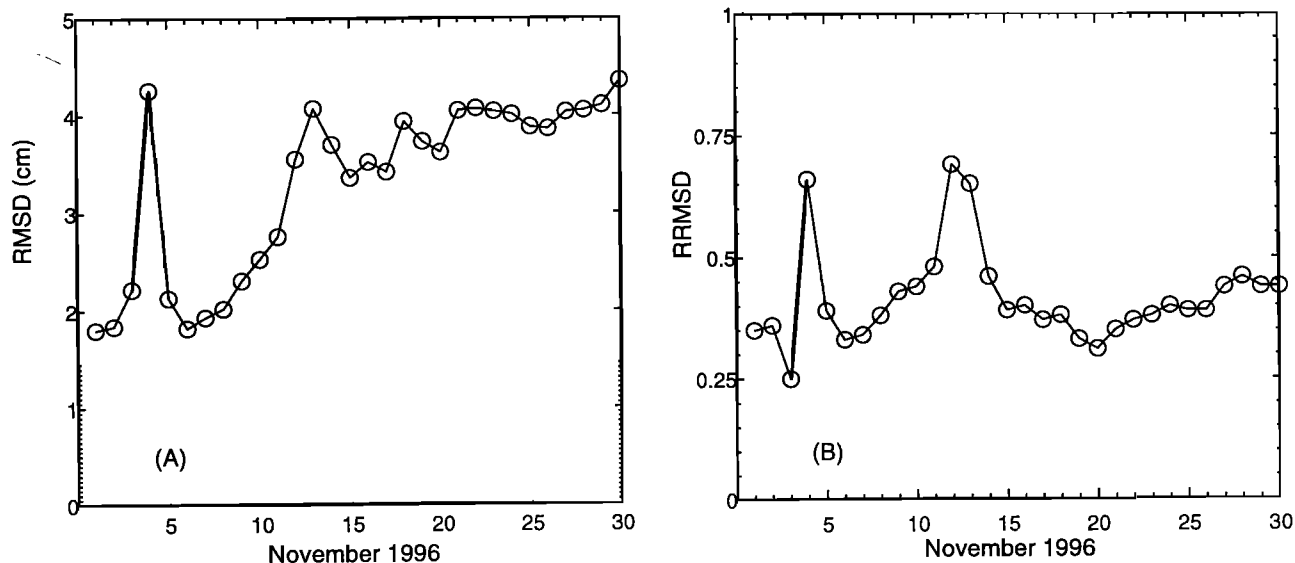**Figure 9.** Same as Figure 7, except for the model surface elevation.

Figure 10. Same as Figure 6 except, for the model surface elevation.

the two runs (NSCAT minus NCEP run) indicates that the NSCAT run has a stronger coastal jet along the southeast Chinese coast, a cyclonic circulation near the Luzon Strait, and a strong divergence in southern SCS near Borneo. On November 15, Ernie was approaching the Vietnamese coast (Figure 4). Both runs simulate a strong coastal jet all the way from the Taiwan Strait to Karimata Strait. The NCEP run shows a much stronger eastern boundary flow along the west coast of Borneo-Palawan.

Figure 13a shows the rmsd for currents at three different σ levels: 0, -0.025, and −0.1. The rmsd generally decreased with depth and increased with time. The highest rmsd is 18 cm s^{-1}, occurring at the surface on November 30 (Table 3). The lowest rmsd is 3 cm s^{-1}, occurring at $\sigma = -0.1$ on November 1.
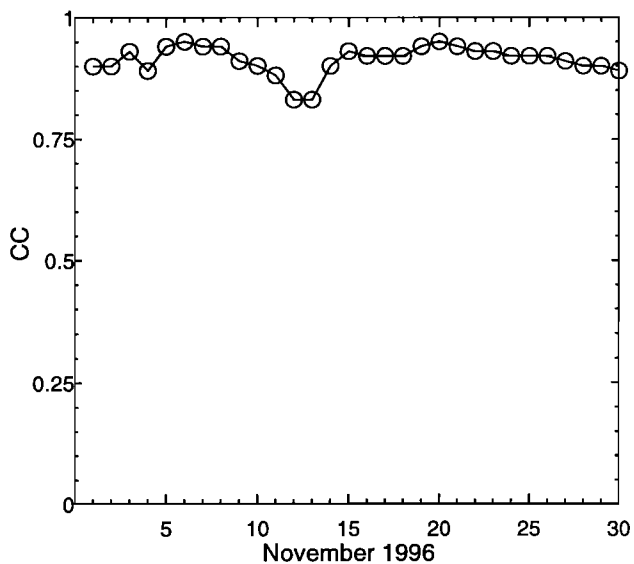

Figure 11. Correlation coefficient between NSCAT and NCEP model surface elevation.

Figure 13b shows the rrmsd for currents at the three σ levels. For a given σ level the rrmsd increased from its minimum value (e.g., 0.47 at the surface) on November 1 to a maximum value (e.g., 1.02 at the surface) on November 4 (Table 4). This maximum value may be due to the monsoon reversal. After November 4, it had a time-decreasing tendency with some fluctuation. On November 30, the rrmsd becomes 0.6 at the surface. Thus the discrepancy of the surface currents caused by the uncertainty in the wind forcing accounts for 60-100% of the internal variability.

Figures 14a and 14b show the CC for the u, v components, respectively, at the three σ levels. The CC generally increased with depth. The lowest CC occurred at the surface on November 4 for both components: CC = 0.59 for the u component (Table 5) and CC = 0.68 for the v component. The minimum CC for the u, v components on November 4 is due to the differences caused by the boundary currents.

6.3. Temperature

Figure 15 shows the comparison between two SST fields under NSCAT and NCEP wind forcing on November 4, 12, and 15. On November 4, 1996, both runs simulated a typical November SST pattern [*Chu et al.*, 1997b], cool water in the northern SCS near the Chinese to northern Vietnamese coasts and warm water (28°C) in the deep SCS basin. The difference between the two runs was negligible. When Ernie was located at the north tip of Luzon on November 12, both runs showed surface cooling (1°C decrease from November 4) in the central SCS between 10° and 16°N. The difference between the two runs becomes larger.

Figure 16a shows the rmsd for temperature at three different σ levels: 0, −0.025, and −0.1. It is interesting to see that the rmsd increased with depth from the
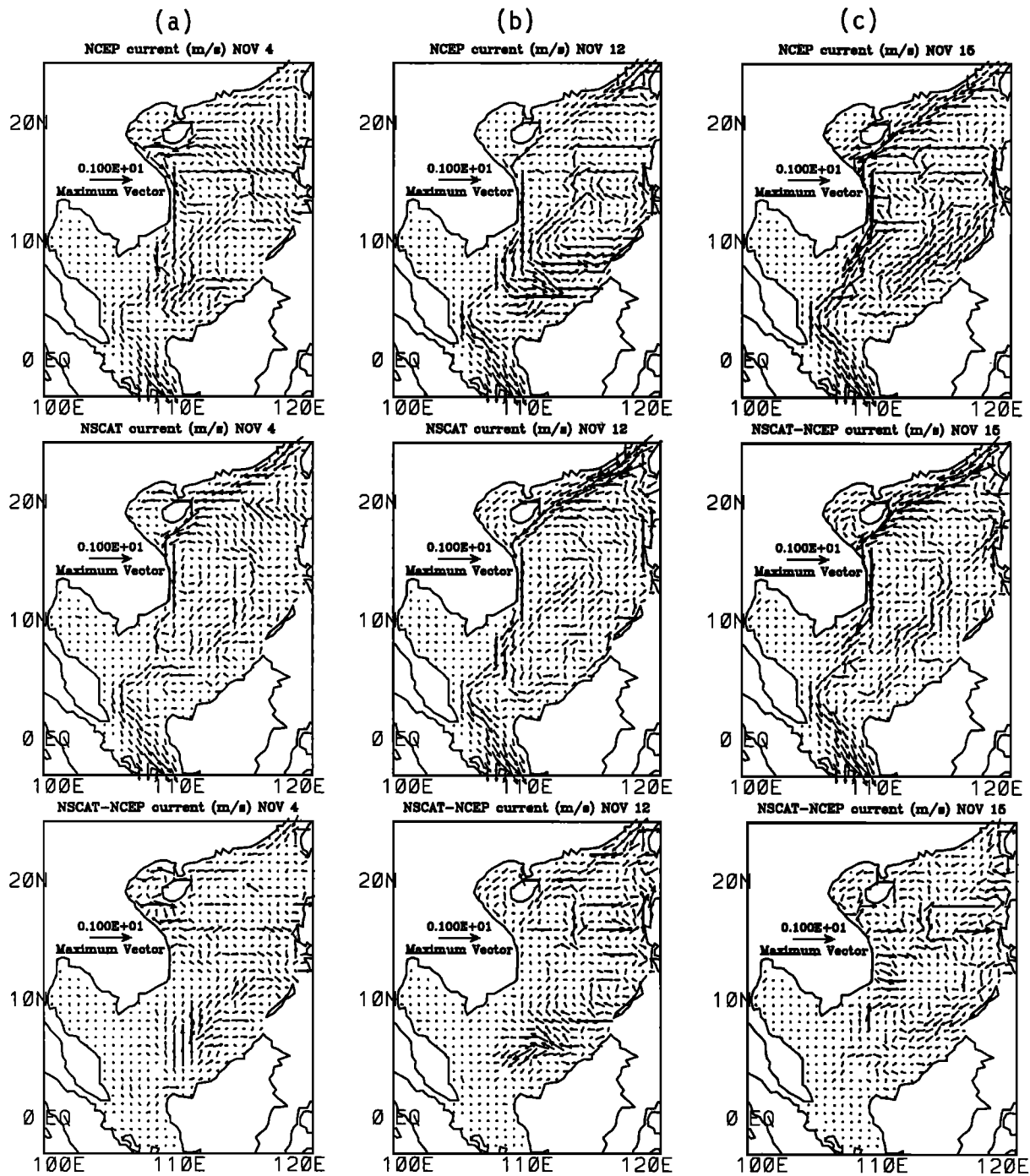
Figure 12. Comparison of the model surface current vectors under NSCAT and NCEP wind forcing on November (a) 4, (b) 12, and (c) 15.
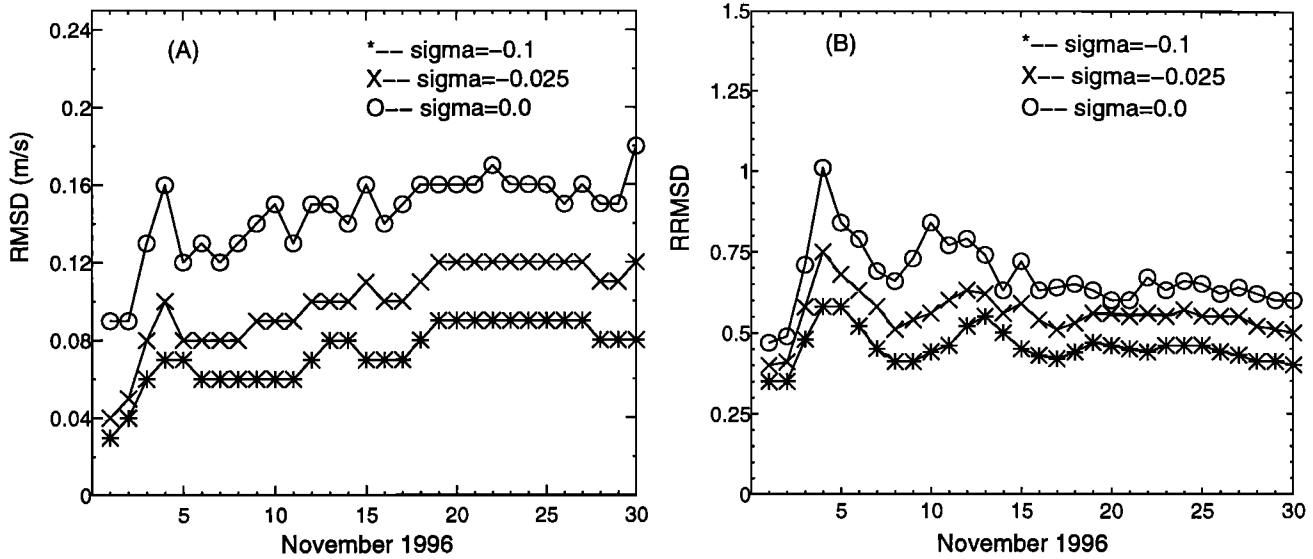
Figure 13. Temporally varying (a) rmsd and (b) rrmsd of the model currents at different σ levels under NSCAT and NCEP wind forcing.

surface to a subsurface level ($\sigma = -0.025$) and then decreased with depth. Tthat the largest rmsd occurred at the subsurface rather than at the surface might be caused by the use of the restoring-type surface thermal forcing. The highest rmsd is 0.52°C, occurring at the subsurface ($\sigma = -0.025$) on November 30 (Table 3.) The lowest rmsd (0.03°C) occurred on the first day of the experiment (November 1).

Figure 16b shows the rrmsd for temperature at the three σ levels. The rrmsd generally decreased with depth and increased with time until November 18 and then leveled off after that day. The rrmsd has a maximum value of 0.23 at the surface on November 18 (Table 4.)

Figure 17 shows the CC for the temperature field at the three σ levels. The values of CC are all quite high (≥ 0.97). The relatively low values of rrmsd (maximum value, 0.23) and high values of CC indicate that the discrepancy of the temperature field caused by the uncertainty in the wind forcing is much smaller than the other parameters such as surface elevation and currents.

7. Conclusions

We investigated the model uncertainty due to the uncertainty of the surface boundary conditions using the POM with 20 km horizontal resolution and 23 σ levels conforming to a realistic bottom topography during
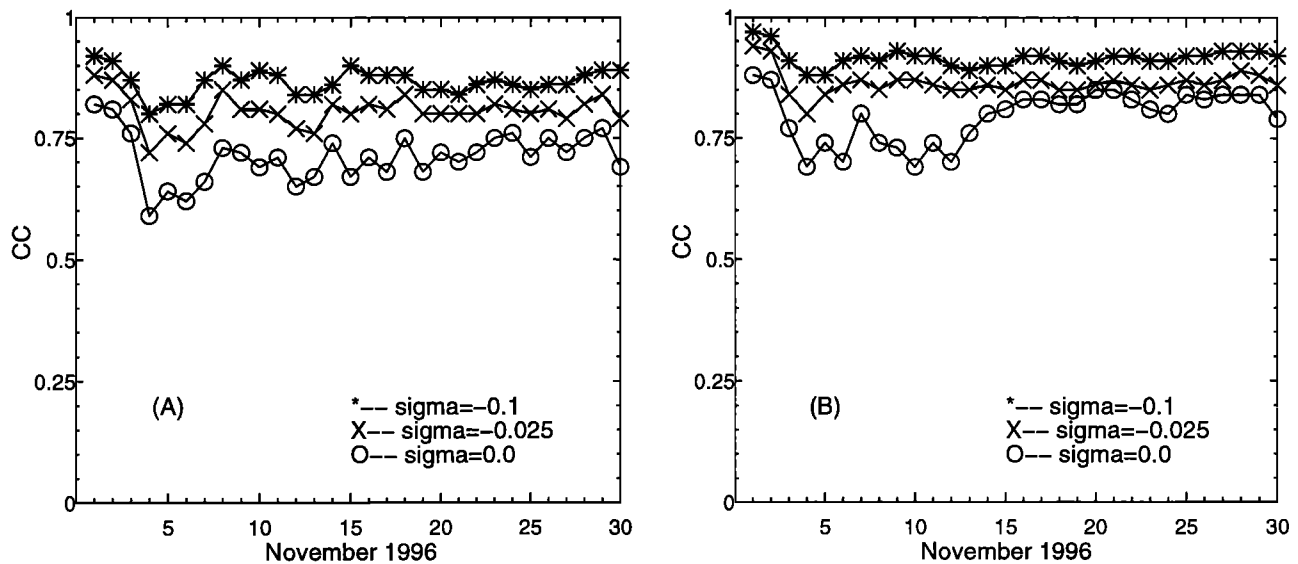

Figure 14. Correlation coefficient of the model currents at different σ levels under NSCAT and NCEP wind forcing for (a) u and (b) v components.
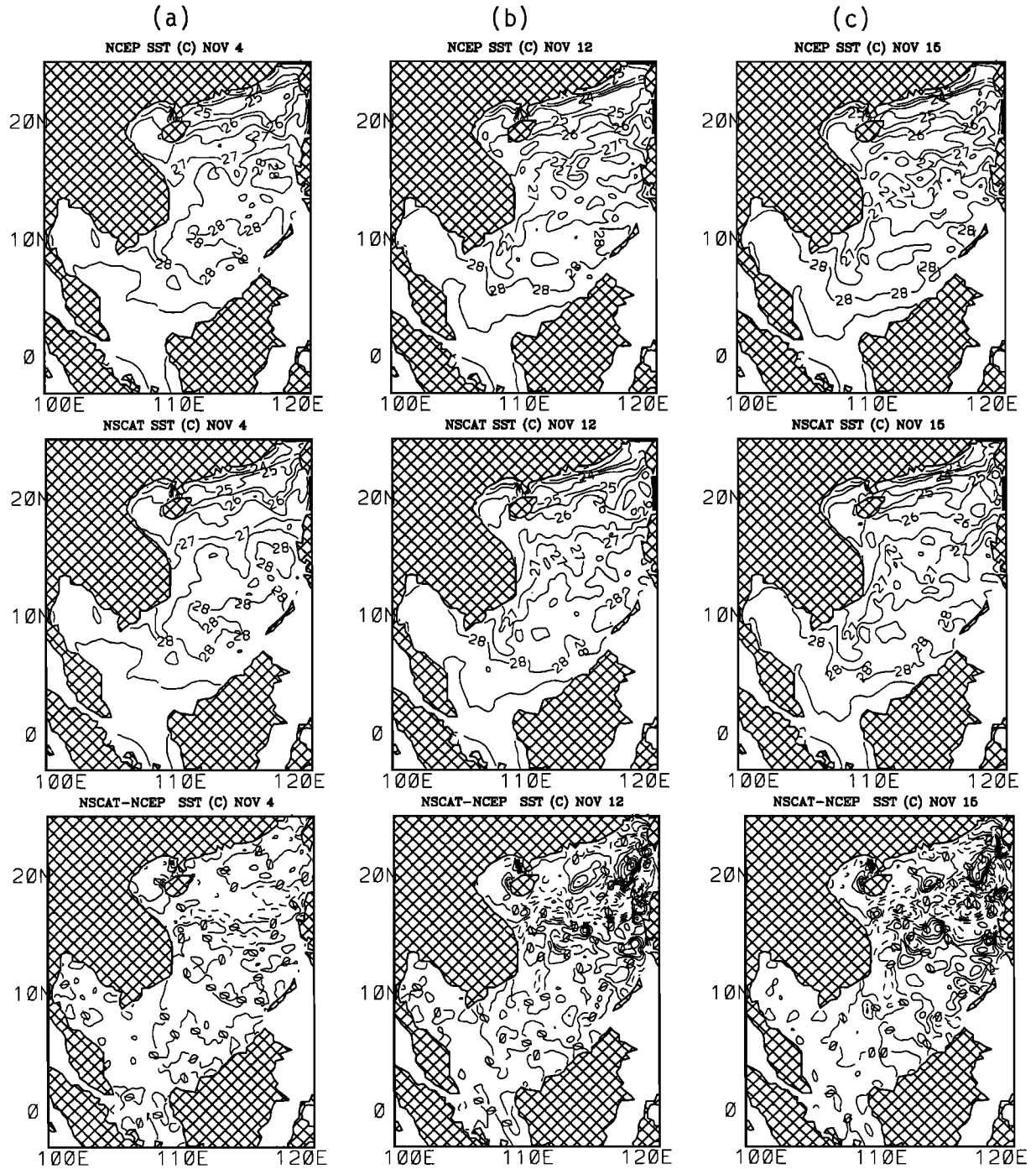
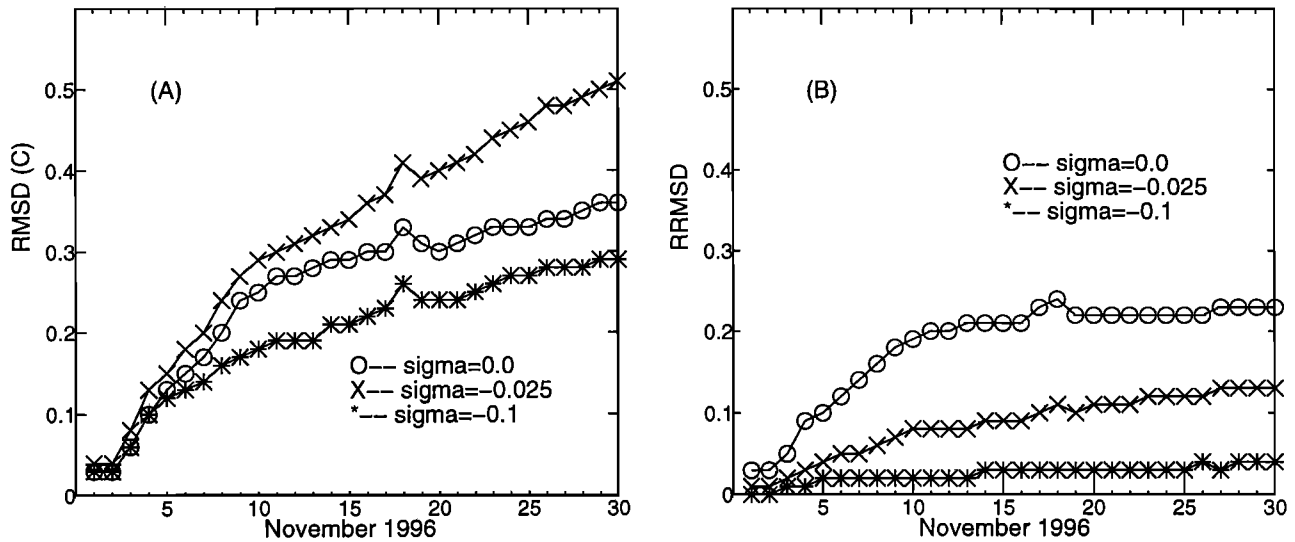**Figure 15.** Same as Figure 12, except for the model temperature.

Figure 16. Same as Figure 13, except for the model temperature.

the lifetime of tropical cyclone Ernie (November 4-18, 1996). The uncertainty of SCS response to the two wind data sets was analyzed by root-mean-square difference, relative root-mean-square difference, and correlation coefficient. Discrepancy between two data sets is characterized by high values of root-mean-square difference and low values of correlation coefficient. After analyzing the discrepancy in two wind data sets (NSCAT and NCEP) and two sets of model output generated using these wind fields, we found the following results.

1. The difference between NSCAT and NCEP winds is not negligible. The root-mean-square difference increased from 3.6 m s^{-1} on November 1 to a maximum value of 6.7 m s^{-1} on November 4, 1996, the day when the boundary current was strongest, and then fluctuated afterward between 6.7 and 2.7 m s^{-1}. It varies from 50 to 100% of the internal wind variability and

Figure 17. Correlation coefficient of model temperature.

equals the internal wind variability on November 12. The correlation coefficient fluctuated between 0.6 and 0.9 for the u component and between 0.42 and 0.92 for the v component. The minimum correlation coefficient was found to be as low as 0.42 for the latitudinal component on November 4, 1996.

2. The uncertainty in surface winds generated uncertainty in surface elevation. The root-mean-square difference of surface elevation between NSCAT and NCEP runs increased with time and had a maximum value of 4.3 cm on November 4 and 30, 1996. It varied from 25 to 70% of the internal variability of the surface elevation. The correlation coefficient of surface elevation between the two runs fluctuated between 0.81 and 0.96.

3. The uncertainty in surface winds generated uncertainty in currents. The root-mean-square difference of currents between NSCAT and NCEP runs decreased with depth, increased with time, and had a maximum value of 18 cm s^{-1}, occurring at the surface on November 30. It varied from 47 to 102% of the internal variability of the surface currents. The correlation coefficient of currents between the two runs generally increased with depth. The lowest value occurred at the surface on November 4 for both the u (0.59) and v components (0.68).

4. The uncertainty in surface winds generated uncertainty in temperature. The root-mean-square difference of temperature between NSCAT and NCEP runs increased with depth from the surface to a subsurface level ($\sigma = -0.025$) and then decreased with depth. It had a maximum value of 0.52°C at $\sigma = -0.025$ on November 30, 1996. It varied from a few per cent up to 23% of the internal temperature variability. The correlation coefficient of temperature between two runs is quite high (0.97-1.0). The relatively low values of relative root-mean-square difference (maximum value, 0.23) and high values of correlation coefficient indicate that
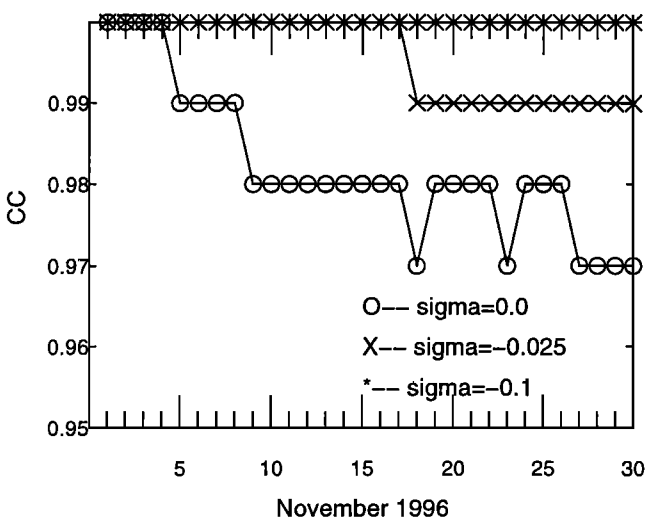
the discrepancy of the temperature field caused by the uncertainty in the wind forcing is much smaller than the other parameters such as surface elevation and currents.

5. The relative root-mean-square difference of two winds or of two model results is a useful uncertainty index. This index for the model variables such as current and temperature always decreases with depth. Furthermore, this index is usually smaller in the model results (0.25 to 0.7 for surface elevation, 0.47 to 1.02 for surface current, and less than 0.23 for temperature) than in the winds (0.5 to 1.0). We may conclude that the model has less uncertainty overall than the wind fields used to drive it. This suggests that the ocean modeling community may progress without waiting for the atmospheric modelers to build the perfect forecast model.

References

Blumberg, A. F., and G. L. Mellor, A description of a three-dimensional coastal ocean circulation model, in *Three Dimensional Coastal Ocean Models, Coastal and Estuarine Sciences*, vol. 4, edited by N.S. Heaps, pp.1-16, AGU, Washington, D. C., 1987.

Chu, P. C., C. C. Li, D. S. Ko, and C. N. K. Mooers, Response of the South China Sea to seasonal monsoon forcing, in *Proceedings of the Second International Conference on Air-Sea Interaction and Meteorology and Oceanography of the Coastal Zone*, pp. 214-215, Am. Meteorol. Soc., Boston, Mass., 1994.

Chu, P. C. , M. Huang, and E. Fu, Formation of the South China Sea warm core eddy in boreal spring, in *Proceedings of the Eighth Conference on Air-Sea Interaction*, pp.155-159, Am. Meteorol. Soc., Boston, Mass., 1996.

Chu, P. C., H. C. Tseng, J. M., Chen, and C. P. Chang, South China Sea warm pool detected from the Navy's Master Oceanographic Observational Data Set, *J. Geophys. Res.*, *102*, 15,761-15,771, 1997a.

Chu, P.C., S. H. Lu, and Y.C. Chen, Temporal and spatial variability of the South China Sea surface temperature anomaly, *J. Geophys. Res.*, *102*, 20,937-20,955, 1997b.

Chu, P.C., C. Fan, C.J. Lozano, and J.L. Kirling, An airborne expendable bathythermograph survey of the South

China Sea, May 1995, *J. Geophys. Res.*, *103*, 21,637-21,652, 1998a.

Chu, P.C., S. H. Lu, and Y.C. Chen, Wind-driven South China Sea deep basin warm-core/cool-core eddies, *J. Oceanogr.*, *54*, 347-360, 1998b.

Dale, W.L., Winds and drift currents in the South China Sea, *Malays. J. Trop. Geogr.*, *8*, 1-31, 1956.

Gray, W.M., Global view of the origin of tropical disturbances and storms, *Mon. Weather Rev.*, 96, 669-700, 1968.

Haney, R.L., Surface boundary conditions for ocean circulation models, *J. Phys. Oceanogr.*, 1, 241-248, 1971.

Hellerman, S., and M. Rosenstein, Normal monthly wind stress over the world ocean with error estimates, *J. Phys. Oceanogr.*, *13*, 1093-1104, 1983.

Levitus, S., and T. Boyer, World Ocean Atlas, vol. 4, Temperature, *NOAA Atlas NESDIS*, *4*, 117 pp., U.S. Gov. Print. Off., Washington, D.C., 1994.

Levitus, S., R. Burgett, and T. Boyer, World Ocean Atlas, vol. 3, Salinity, *NOAA Atlas NESDIS*, *3*, 99 pp., U.S. Gov. Print. Off., Washington, D.C., 1994.

Liu, W.T., W. Tang, and P.S. Polito, NASA scatterometer provides global ocean-surface wind fields with more structures than numerical weather prediction, *Geophys. Res. Lett.*, *25*, 761-764, 1998.

McBride, J. L., Tropical cyclone formation, in *Global Perspectives of Tropical Cyclones, Tech. Doc. 693*, edited by R. L. Elsberry, pp.63-102, World Meteorol. Organ., Geneva, 1995.

Mellor, G.L., and T. Yamada, Development of a turbulence closure model for geophysical fluid problems, *Rev. Geophys. Space Phys.*, *20*, 851-875, 1982.

Metzger, E. J., and H. Hurlburt, Coupled dynamics of the South China Sea, the Sulu Sea, and the Pacific Ocean, *J. Geophy. Res.*, *101*, 12,331-12,352, 1996.

Smagorinsky, J., General circulation experiments with the primitive equations, *Mon. Weather Rev.*, *91*, 99-164, 1963.

Tang, W., and W.T. Liu, Objective interpolation of scatterometer winds, *JPL Publ. 96-19*, pp. 1-16, Jet Propul. Lab., Pasadena, Calif., 1996.

Wyrtki, K., Scientific results of marine investigations of the South China Sea and Gulf of Thailand 1959-1961, *Naga Rep.*, *2*, pp. 164-169, Scripps Institution of Oceanography, University of California, San Diego, 1961.

P. C. Chu, Department of Oceanography, Naval Postgraduate School, Monterey, CA 93943 (e-mail: chu@nps.navy.mil)

W. T. Liu, Jet Propulsion Laboratory, Pasadena, CA 91109

S. Lu, Institute of Plateau Atmospheric Physics, Academia Sinica, Lanzhou, China